78

SATELLITE & MESOMETEOROLOGY RESEARCH PROJECT

Department of the Geophysical Sciences
The University of Chicago

FORMATION AND STRUCTURE OF EQUATORIAL ANTICYCLONES
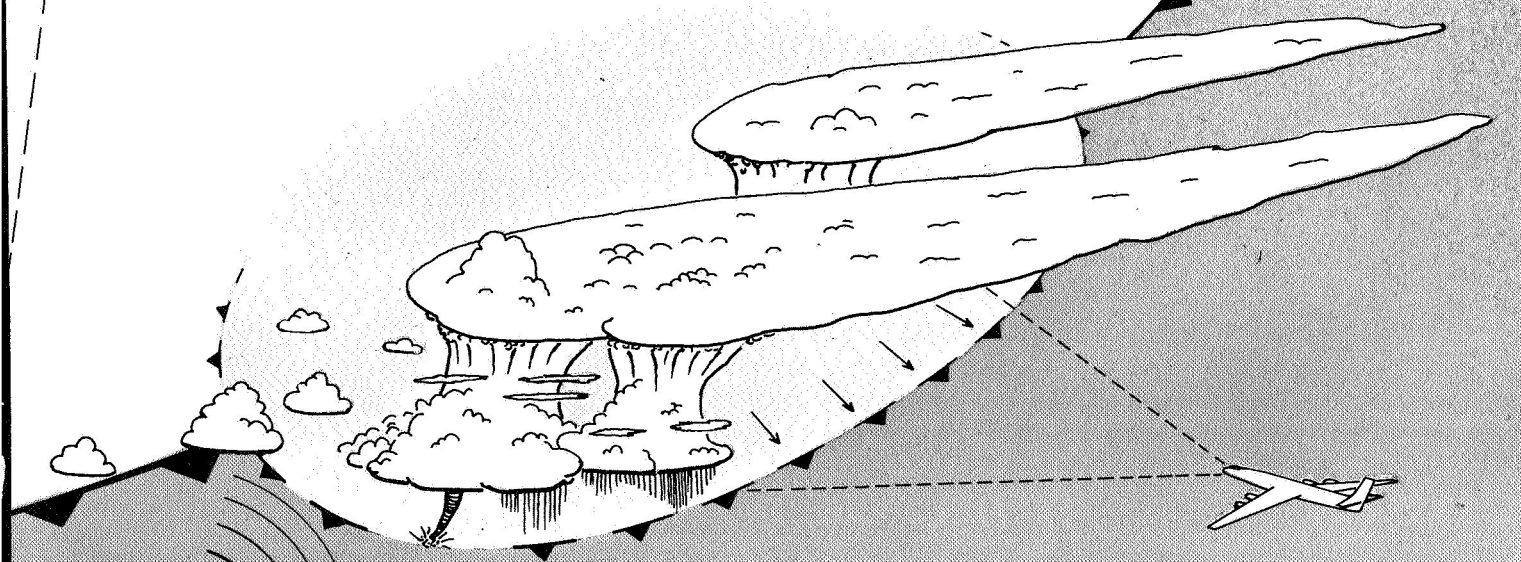CAUSED BY LARGE-SCALE CROSS EQUATORIAL FLOWS
DETERMINED BY ATS-I PHOTOGRAPHS

by

Tetsuya T. Fujita
The University of Chicago

and

Kazuo Watanabe and Tatsuo Izawa
Meteorological Research Institute, Tokyo

CASE FILE
COPY

SMRP Research Paper
NUMBER   78

January   1969

MESOMETEOROLOGY PROJECT --- RESEARCH PAPERS

1.*   Report on the Chicago Tornado of March 4, 1961 - Rodger A. Brown and Tetsuya Fujita

2.*   Index to the NSSP Surface Network - Tetsuya Fujita

3.*   Outline of a Technique for Precise Rectification of Satellite Cloud Photographs - Tetsuya Fujita

4.*   Horizontal Structure of Mountain Winds - Henry A. Brown

5.*   An Investigation of Developmental Processes of the Wake Depression Through Excess Pressure Analysis of Nocturnal Showers - Joseph L. Goldman

6.*   Precipitation in the 1960 Flagstaff Mesometeorological Network - Kenneth A. Styber

7.**   On a Method of Single- and Dual-Image Photogrammetry of Panoramic Aerial Photographs - Tetsuya Fujita

8.   A Review of Researches on Analytical Mesometeorology - Tetsuya Fujita

9.*   Meteorological Interpretations of Convective Nephsystems Appearing in TIROS Cloud Photographs - Tetsuya Fujita, Toshimitsu Ushijima, William A. Hass, and George T. Dellert, Jr.

10.*   Study of the Development of Prefrontal Squall-Systems Using NSSP Network Data - Joseph L. Goldman

11.   Analysis of Selected Aircraft Data from NSSP Operation, 1962 - Tetsuya Fujita

12.   Study of a Long Condensation Trail Photographed by TIROS I - Toshimitsu Ushijima

13.   A Technique for Precise Analysis of Satellite Data; Volume I - Photogrammetry (Published as MSL Report No. 14) - Tetsuya Fujita

14.   Investigation of a Summer Jet Stream Using TIROS and Aerological Data - Kozo Ninomiya

15.   Outline of a Theory and Examples for Precise Analysis of Satellite Radiation Data - Tetsuya Fujita

16.   Preliminary Result of Analysis of the Cumulonimbus Cloud of April 21, 1961 - Tetsuya Fujita and James Arnold

17.   A Technique for Precise Analysis of Satellite Photographs - Tetsuya Fujita

18.*   Evaluation of Limb Darkening from TIROS III Radiation Data - S.H.H. Larsen, Tetsuya Fujita, and W.L. Fletcher

19.   Synoptic Interpretation of TIROS III Measurements of Infrared Radiation - Finn Pedersen and Tetsuya Fujita

20.*   TIROS III Measurements of Terrestrial Radiation and Reflected and Scattered Solar Radiation - S.H.H. Larsen, Tetsuya Fujita, and W.L. Fletcher

21.   On the Low-level Structure of a Squall Line - Henry A. Brown

22.*   Thunderstorms and the Low-level Jet - William D. Bonner

23.*   The Mesoanalysis of an Organized Convective System - Henry A. Brown

24.   Preliminary Radar and Photogrammetric Study of the Illinois Tornadoes of April 17 and 22, 1963 - Joseph L. Goldman and Tetsuya Fujita

25.   Use of TIROS Pictures for Studies of the Internal Structure of Tropical Storms - Tetsuya Fujita with Rectified Pictures from TIROS I Orbit 125, R/O 128 - Toshimitsu Ushijima

26.   An Experiment in the Determination of Geostrophic and Isallobaric Winds from NSSP Pressure Data - William Bonner

27.   Proposed Mechanism of Hook Echo Formation - Tetsuya Fujita with a Preliminary Mesosynoptic Analysis of Tornado Cyclone Case of May 26, 1963 - Tetsuya Fujita and Robbi Stuhmer

28.   The Decaying Stage of Hurricane Anna of July 1961 as Portrayed by TIROS Cloud Photographs and Infrared Radiation from the Top of the Storm - Tetsuya Fujita and James Arnold

29.   A Technique for Precise Analysis of Satellite Data, Volume II - Radiation Analysis, Section 6. Fixed-Position Scanning - Tetsuya Fujita

30.   Evaluation of Errors in the Graphical Rectification of Satellite Photographs - Tetsuya Fujita

31.   Tables of Scan Nadir and Horizontal Angles - William D. Bonner

32.   A Simplified Grid Technique for Determining Scan Lines Generated by the TIROS Scanning Radiometer - James E. Arnold

33.   A Study of Cumulus Clouds over the Flagstaff Research Network with the Use of U-2 Photographs - Dorothy L. Bradbury and Tetsuya Fujita

34.   The Scanning Printer and Its Application to Detailed Analysis of Satellite Radiation Data - Tetsuya Fujita

35.   Synoptic Study of Cold Air Outbreak over the Mediterranean using Satellite Photographs and Radiation Data - Aasmund Rabbe and Tetsuya Fujita

36.   Accurate Calibration of Doppler Winds for their use in the Computation of Mesoscale Wind Fields - Tetsuya Fujita

37.   Proposed Operation of Intrumented Aircraft for Research on Moisture Fronts and Wake Depressions - Tetsuya Fujita and Dorothy L. Bradbury

38.   Statistical and Kinematical Properties of the Low-level Jet Stream - William D. Bonner

39.   The Illinois Tornadoes of 17 and 22 April 1963 - Joseph L. Goldman

40.   Resolution of the Nimbus High Resolution Infrared Radiometer - Tetsuya Fujita and William R. Bandeen

41.   On the Determination of the Exchange Coefficients in Convective Clouds - Rodger A. Brown

      *   Out of Print
      **   To be published

SATELLITE AND MESOMETEOROLOGY RESEARCH PROJECT

Department of the Geophysical Sciences

The University of Chicago

FORMATION AND STRUCTURE OF EQUATORIAL ANTICYCLONES
CAUSED BY LARGE-SCALE CROSS-EQUATORIAL FLOWS
DETERMINED BY ATS-I PHOTOGRAPHS

by

Tetsuya T. Fujita
The University of Chicago

and

Kazuo Watanabe and Tatsuo Izawa
Meteorological Research Institute, Tokyo

SMRP Research Paper No. 78

January 1969

FORMATION AND STRUCTURE OF EQUATORIAL ANTICYCLONES CAUSED BY LARGE-SCALE CROSS-EQUATORIAL FLOWS DETERMINED BY ATS-I PHOTOGRAPHS[1]

by

Tetsuya T. Fujita
The University of Chicago

and

Kazuo Watanabe and Tatsuo Izawa
Meteorological Research Institute, Tokyo

ABSTRACT

Because of poor coverage by synoptic stations, the tropical circulation over the eastern Pacific has not been known too well. As a result of photographic experiments, using geosynchronous ATS-I, fields of cloud motion over the eastern equatorial Pacific were mapped in detail on a number of days in September 1967. It was found that a large-scale flow from the Southern Hemisphere recurves after crossing the equator to form an anticyclone centered around 10N. Dynamical characteristics of this type of anticyclone were investigated by estimating the vorticity dissipating force from computed values of divergence and vorticity of low-cloud velocities determined from successive ATS-I pictures. The vorticity dissipating force seems to be related closely to the sea-surface temperature which would reduce the frictional coupling between the low-level atmosphere and the underlying sea surface. It was found that the anticyclone in its development stage results in a discontinuity of the intertropical band of cloudiness; then it travels westward, accompanying an active cloud band along its leading edge. Based upon evidence found through case studies, a model of an equatorial anticyclone is proposed in this paper. Numerical computations of cross-

---

equatorial trajectories were performed by using the divergence-vorticity relationships and the vorticity dissipating force, which were obtained through numerical analyses. This paper thus presents an initial step toward the further development of tropical synoptic meteorology, which is expected during the next few years as a result of photographic experiments by using ATS-I and III.

1. Introduction

Advanced knowledge of meteorological disturbances in high latitudes has been applied, during the past two decades, to the tropics so as to improve our understanding and subsequent forecasting of tropical weather systems. The lack of significant gradients in meteorological parameters in the deep tropics except in the areas of tropical storms made it very difficult for us to establish the fields of pressure and temperature related to the patterns of cloudiness. Meteorologists, therefore, tend to analyze streamlines based upon few island-station reports and those by ships.

Analyses of tropical flow patterns by Palmer (1952) convincingly clarified the existence of equatorial and easterly waves which often develop into tropical storms. Extensive discussion by Riehl (1954) in his book Tropical Meteorology also supported the existence of easterly waves in the Caribbean area.

In pre-satellite days, a band of cloudiness running parallel to the equator was studied both climatologically and synoptically. The band called the "intertropical convergence zone (ITCZ)" has been regarded as a zone in which the southeast trades and the northeast trades of the Southern and Northern Hemispheres, respectively, converge to form a well-defined band.

Because the cloudiness associated with ITCZ broadens when easterly waves develop, the relationships between cloud patterns in satellite pictures and easterly waves in various stages were studied by a number of researchers, resulting occasionally in arguments leading to proposed revisions of the term ITCZ. There is no doubt that we see a climatological band or bands of cloudiness as studied by Godshall (1967) and Kornfield, et. al. (1967). In individual pictures, however, the cloud patterns appear to be characterized by several large nephsystems, 5- to 10-degrees across, distributed in the form of a band.

Their average distance varies between 10 and 30 degrees, thus giving an impression that it is close to the 2000-km wavelength of the easterly waves mentioned earlier.

During the JOC Meeting[2], the term "cloud cluster" was adopted for these large nephsystems which are also called blobs, cells, etc. Due to the lack of synoptic data, however, the dynamical characteristics of cloud clusters have not been clarified.

As a result of photographic experiments using both ATS-I and III, we are now able to determine velocities of clouds within few knot accuracy. About 25 velocities can be computed inside each 10 x 10 degree square near the subsatellite point. These velocities, carefully sorted according to the consistency of velocity field, would represent flow patterns either at the inflow or the outflow level. Some results of synoptic and dynamical analyses of equatorial regions will be presented in this paper.

2. Computation of Cloud Velocities from ATS-I Pictures

Since our initial interest is to relate the patterns of large clouds with the field of small-cloud velocities, a series of ATS-I pictures was used to determine the displacement of each cloud. A cloud to be tracked was so selected that, 1) its life is long enough to cover the entire tracking period of about two hours or that of five pictures, and that 2) the cloud is no more than 15 miles across, showing both cellular and low-cloud characteristics. After the selection of a large number of cloud elements satisfying the above conditions, the geometric center of each element was tracked by using a loop projector. For details refer to Fujita and Bradbury (1968) who determined ATS cloud velocities for their comparison with those obtained from terrestrial stereo-pair pictures. Our tracking accuracy is about 5 n.m. or about 10 km so that a displacement vector for a two-hour period can be determined with an accuracy of 2.5 kt near the subsatellite point at 151W at the equator for ATS-I in September 1967, the month of our research.

Figure 1 shows the distribution of cloud velocities obtained from a series of six ATS pictures started, respectively, at 1948, 2011, 2035, 2102, 2129, and 2152Z, September 17, 1967. These cloud velocities were determined on ATS pictures and then transferred to an ESSA digital mosaic on Mercator projection. The length of the arrow is drawn to be proportional to the measured cloud velocity while open circles denote those

---

[2]Report on the first session of the Study Group on Tropical Disturbances (Madison, Wisconsin, October 21-November 8, 1968) Joint GARP Organization Committee, WMO.

cloud elements which did not move during this tracking period.

There are three tropical cyclones, Nanette, Monica, and Beulah in the picture along about 20N latitude. Due to a well-established outflow from Beulah, the top of Monica was under the influence of moderate east-southeasterlies which continued over to the region of Nanette. Velocities of high clouds imbedded in this outflow are not entered in Fig. 1 which is prepared to show the field of low-cloud velocities.

A serious problem in utilizing an ATS picture series in determining the field of low-cloud velocities is that we cannot see pieces of low clouds located beneath canopies over clusters of convective cells. It is necessary, therefore, to interpolate and estimate the velocity field beneath these canopies from that outside the canopy areas. Because of the evidence that the cloud-velocity disturbance associated with a cloud cluster extends far away from the canopy area, it is usually feasible to establish the field of low-cloud velocities related to intertropical cloud patterns.

Streamlines of low-cloud velocities were drawn in Fig. 2 which also includes boundaries of large nephsystems. Three significant points, such as discussed by Riehl (1954), were used in describing the cloud-velocity field. They are the points where air is calm, which are classified as the cyclonic circulation center (a black dot), the anticyclonic circulation center (a small open circle), and the saddle point (a cross symbol). A line of directional convergence toward which streamlines converge is indicated by a heavy dashed line.

Examination of flow patterns in relation to nephsystems reveals that the cyclonic circulation center coincides with those of tropical storms. The cyclonic circulation centers seem to be related physically to large cloud clusters nearby. It is of interest to find that an anticyclone "A" is located over a clear area separating the intertropical cloud band into two. These subjects will be discussed later.

3. Correction of Semidiurnal Pressure Variation and Surface-Map Analyses

After the determination of the field of low-cloud velocities in the previous section we shall compare the field with that of low-level winds. It is highly desirable to make such a comparison at several levels in the lower layers of the atmosphere; however, because

of the lack of upper-air stations over the area of interest, only surface maps were available
for comparison with the cloud-velocity field.

Shown in Fig. 3 is an example of these surface maps analyzed by plotting all
available ship and station reports. In order to increase data over the ocean, surface
winds reported by ships 6 hours before and after the synoptic time were also plotted at
the ship positions without station circles.

Due to the fact that semi-diurnal pressure variation, decreasing poleward, reaches
as large as 4 mb in full amplitude at the equator, and that observed surface winds do not
adjust themselves to this passing pressure wave of 20,000 km wavelength travelling at
about 1,700 km hr^{-1}, all surface pressures were plotted after correcting the semi-diurnal
variations. No corrections to diurnal variation were made in this case because its
amplitude is rather small over the ocean areas where diurnal temperature variation
is insignificant.

Drawn in OOZ, September 18, 1967 chart (see Fig. 3) are isobars for pressures
after semi-diurnal variation correction and streamlines of surface winds. Two tropical
storms, Nanette and Monica and hurricane Beulah are clearly depicted. Since the period
of cloud-velocity computed used in Figs. 1 and 2 is only 2 to 4 hours earlier than the time
of the surface map in Fig. 3, we may compare these three figures for further meteorolo-
gical interpretation. An anticyclone centered at 10N and 120W appears in all three figures.
Note that the wind circling anticyclonically around the center can be traced back across
the equator toward the region off Chile. This is the southeast wind from the middle-
latitude high over the south Pacific.

Although it is not possible to estimate the height of the flow represented by low-cloud
velocities determined from ATS pictures, cloud-velocity field is very close to the field of
surface wind. A number of other studies by Fujita[3] indicated that low-cloud velocities
are very close to the winds at about 3,000-ft. In other words, cellular clouds in the

---

[3] Lectures on the use of ATS pictures entitled: Mesostructure of Subtropical Jet-
Stream, Growth of Anvil Clouds, Modification of Jetstream by Large Convective Storms,
Outflow from a Large Tropical Cloud Mass, Kinematic Analysis of Hurricane Brenda,
and Divergence and Vorticity at the Jetstream Level. Presented at the WMO Training
Seminar on Interpretation of Meteorological Satellite Data, Melbourne, Australia,
November-December, 1968.

tropics move with the wind approximately at the cloud base. Hubert and Whitney[4] found, on the other hand, that low-cloud velocity agrees best with the 6000-ft wind. Figure 2 readily shows that these clusters identified as b, c, and d are located, respectively, to the southeast of cyclonic circulation centers B, C, and D. These locations of cloud clusters are characterized by converging streamlines with cyclonic curvatures, suggesting that absolute voriticity will be very large. If we assume the conservation of potential vorticity while travelling inside each of the cyclonic disturbances, ΔP, the pressure difference between the top and the base of the inflow layer would be very large where Q, the absolute vorticity reaches a maximum. In light of such a simplified dynamical characteristic we may conclude that a band of intertropical cloudiness is composed of several cloud clusters each of which is closely related to the low-level disturbance such as B, C, and D which are spaced more or less evenly. In this case, the spacing was about 1,100 km which is about one-half of equatorial waves as introduced by Palmer (1952).

4. Low-Level Wind Field in Relation to Intertropical Cloud Clusters

It was mentioned earlier that a cloud cluster is embedded inside a low-level wind disturbance extending much beyond its visual boundary. Unless a cirrus canopy obscures low clouds inside the area of the wind disturbance we are able to estimate the field of low-level air motion from computed low-level cloud velocities.

An attempt was made to compute both divergence and relative vorticity from stream-lines in Fig. 2 and isotachs drawn on separate charts. Both direction and speed at each grid point with spacing of 2.5-degree longitude square on a Mercator projection were read out for use as input data.

Divergence patterns of low-level flow, thus computed, are shown in Fig. 4. Isolines are drawn for every 10^{-5} sec^{-1}. When the locations of maximum convergence are compared with those of cloud clusters and intertropical cloud bands, it will be seen that the regions of the maximum convergence are shifted to the southeastern side of these nephsystems.

---

[4]Wind estimate from geostationary satellites presented at New York, AMS Meeting, Jan., 1969. Their analysis of tropical and subtropical cumuli from five different days indicates that 68% are no more than 6 kts and 25° from the 6000-ft wind.

On the other hand, the regions of vorticity maxima shown in Fig. 5 coincide with the positions of cyclonic circulation centers which are located near the northwest edge of the nephsystems under consideration. This means that the locations of vorticity and convergence maxima associated with a cloud cluster are separated by a considerable distance. In the case of a tropical storm, however, both maxima are located near the storm's circulation center. Thus the flow pattern accompanying a cloud cluster seems to be quite different from that of tropical storms. Instead it is rather similar to that of a so-called easterly or equatorial wave, although the latter is characterized by a much longer wave length.

To clarify dynamical characteristics of a cloud cluster Fig. 6 was prepared. Both low-level convergence and vorticity are schematically shown. The absolute vorticity with its maximum near the circulation center decreases both in the up-wind and down-wind directions while the maximum convergence is seen to the up-wind side of the maximum vorticity. Such a distribution of convergence with respect to that of vorticity fits to the concept of vorticity advection in relation to divergence. Under the steady-state assumption we write the well-known equation by Petterssen (1956)

$$-V \frac{\partial Q}{\partial s} = DQ \qquad (1)$$

where V denotes the speed of air parcel moving toward the direction s, Q, the absolute vorticity, and D the divergence. This equation shows that large convergence corresponds to the region where the vorticity advection, as defined by the left side of Eq. (1), shows large negative values. The location of maximum convergence in Fig. 6 is where the vorticity advection is significant. Referring to this figure we try to move low-level air enclosed by a rectangular box inside the friction layer toward the region of maximum convergence. The top of the inflow air moves upward while conserving the potential vorticity as soon as the air passes the top of the frictional layer. If the low-level air is sufficiently warm and humid, the top will soon reach the outflow layer at the cirrus level where diverging air spreads the cirrus canopy. Since the air parcel tends to conserve its potential vorticity while advecting into the region of varying absolute vorticity,

the pressure difference between the top and the bottom of the parcel is more or less proportional to the absolute vorticity which increases toward the location of the maximum vorticity. Over the regions of decreasing absolute vorticity, where divergence dominates, convective clouds no longer receive moisture supply from the friction layer, resulting in the disintegration of cirrus canopy along with convective towers. The processes of cloud-cluster circulation are not reversible because it transports a significant amount of moisture, hydrometeors, and air from the friction layer to the outflow layer through condensation processes.

Although the locations of the centers of vorticity, convergence, and cloud clusters do not coincide precisely, the formation of cloud clusters is closely related to the frictional convergence by which the air inside the friction layer is pumped upward to form cirrus canopies. We may expect, therefore, that the grid-point values of vorticity and divergence plotted on a ζ vs. D diagram distribute systematically forming groups of points representing values inside or outside cloud clusters. A scatter diagram for these point values located inside tropical storms, inside cloud clusters, and outside cloud clusters appears in Fig. 7. The diagram reveals that clear areas are characterized by either divergence or very small convergence but mostly by anticyclonic relative vorticity. The areas of cloud clusters are where ζ is positive and D is negative. Grid-point values inside hurricanes are also located inside the same domain where ζ is positive and D is negative.

In connection with the dynamical properties accompanied by cloud clusters which often form a band of cloudiness, we shall discuss proper terms for the intertropical cloudiness which has long been called the "intertropical convergence zone" or ITCZ. In view of the evidence that the cloud band is characterized more by "vorticity" than "convergence", we may call it the "intertropical vorticity zone" or ITVZ. If we refer only to the pattern of clouds we may call it the "intertropical cloud band" ITCB. The ITCB in this definition may be a solid band of cloudiness or a band of cloudiness consisting of a number of cloud clusters.

5. Evaluation of Vorticity Dissipating Force

So far we assumed that potential vorticity can be conserved against convergence. Cressman (1948) computed trajectories of cross-equatorial flow under further assumption of absolute vorticity constant, thus obtaining constant absolute vorticity trajectories (CAVT). These trajectories show significant anticyclonic curvatures as air parcels travel away from the equator.

In their computation of air trajectories over the Indian Ocean, Gordon and Taylor (1966) introduced friction in a linear form

$$\frac{du}{dt} - fv = -\frac{1}{\rho}\frac{\partial P}{\partial x} - ku$$

$$\frac{dv}{dt} + fu = -\frac{1}{\rho}\frac{\partial P}{\partial y} - kv$$

$$(2)$$

where k is a constant of a dimension sec^{-1}. These expressions are very convenient for their trajectory computations due to the fact that isobars over the Indian Ocean are more or less parallel to the equator. Computed trajectories revealed that they vary significantly with input values of k which increases with the frictional coupling between the sea surface and the friction layer.

Now that ATS pictures provide accurate methods of computing cloud-velocity field, we shall try to determine the extent of the frictional coupling. Over the eastern tropical Pacific where equatorial anticyclones form as a result of cross-equatorial flow of the Southern Hemisphere air, there will be no pre-existing high-pressure centers. But the cross-equatorial flows under favorable conditions curve anticyclonically until they form an anticyclonic closed circulation.

To avoid unneccessary complications involving pressure fields, we shall start from the vorticity equation but neglect the solenoid term because of insignificant gradient in temperature and pressure and also neglect the horizontal gradient of vertical motion since we deal only with the flow of the atmosphere inside the friction layer defined by low-cloud velocities. These assumptions are made by Riehl (1954) in simplifying vorticity equations. Now we shall write the vorticity equations under the above assumptions but including the frictional force between the sea surface and the low-level flow, thus

$$\dot{Q} = -QD + \text{rot } \mathbf{F} \tag{3}$$

where $\mathbf{F}$ denotes the frictional force, Q and $\dot{Q}$ are the absolute vorticity and its time derivative, and D, the divergence.

By using the expression of the frictional force in Eq. (2) we may write

$$\dot{Q} = -QD - \text{rot } k\mathbf{V}$$
$$\tag{4}$$
$$= -QD - k\zeta$$

where $\mathbf{V}$ is the velocity of low-level air or that of cellular low clouds, k, a positive constant, ζ , the relative vorticity, and $-k\zeta$, the vorticity dissipating force.

In order to evaluate the magnitude of the frictional force we assume a steady-state flow and express the rotational part of the frictional force in Eq. (3) as

$$\text{rot } \mathbf{F} = \mathbf{V} \cdot \nabla Q + QD \tag{5}$$

which should be proportional to the relative vorticity if Eq. (4) is applicable to the flow under discussion.

Because we already computed both D and ζ for the flow at OOZ, September 18, 1967, it would be of value to calculate rot $\mathbf{F}$ from these values. The absolute vorticity and streamlines presented in Fig. 8 clearly show that the absolute vorticity is negative everywhere south of the equator. Due to cross-equatorial advection the area of the negative absolute vorticity invades northward beyond the equator as far north as about 11N near the 120W meridian. Due mainly to rot $\mathbf{F}$, the absolute potential vorticity is not conserved for such a low-level flow. From this figure, $\mathbf{V} \cdot \nabla Q$ at each 2.5-deg grid point was obtained. Both Q and D are also read out of Figs. 4 and 8.

Figure 9 shows the pattern of rot $\mathbf{F}$ thus computed. It should be noted that rot $\mathbf{F}$

is negative mostly over the area of disturbances characterized by a large positive relative vorticity. A striking resemblance and negative correlation are found when Figs. 9 and 5 are compared. In other words, the areas of cloud clusters and tropical storms coincide with those of large negative value of rot F . Namely, the rate of increase in the vorticity is suppressed inside cloud clusters where the frictional convergence tends to increase vorticity. The rotational part of the frictional force inside cloud clusters is, therefore, acting as a vorticity dissipating force.

Such an important effect of the vorticity dissipating force can be evaluated by a scatter diagram of rot F against the relative vorticity, ζ . Figure 10 was obtained by plotting computed values of rot F and ζ at 2.5 x 2.5-deg grid points located between 5N and 25N latitudes. The corresponding mesh size is about 280 km. Drawn also in the figure are the isolines of k for 1.0, 2.0, 3.0, and 5.0 x 10^{-5} $\sec^{-1}$. The elongated distribution as outlined by an elliptic boundary indicates that the proper k would be about 3 x 10^{-5} $\sec^{-1}$.

This value shows a good agreement with k $= 1.7$ x 10^{-5} $\sec^{-1}$ as estimated earlier by Gordon and Taylor (1966) based upon an entirely different method applied to Indian Ocean data. Through mesoscale analysis of heavy rain situations over Japan, Mats'umoto and Akiyama[5] determined k to be 4.2 x $10^{-5}$$\sec^{-1}$.

6. Computations of Cross-Equatorial Trajectories

In order to reveal the mechanism of the formation of equatorial anticyclones due to the cross-equatorial flow of low-level wind, we shall compute trajectories in a similar manner to that by Cressman (1948) and Riehl (1954). The only difference is that we added a vorticity dissipating force introduced in the previous section.

The basic equations for computation are derived from Eq. (4) under the steady-state assumption, thus

[5]Personal communication on the result of mesoscale analysis of heavy rainfalls of July 9, 1967.

$$V \cdot \nabla Q = -QD - k\zeta. \tag{6}$$

Then we rewrite this equation in the natural coordinates with s axis toward the direction of motion and n axis pointing left, perpendicular to s axis in a form,

$$V \frac{\partial}{\partial s}(f+\zeta) + (f+\zeta)D + k\zeta = 0 \tag{7}$$

where $f + \zeta = Q$ denotes absolute vorticity.

To carry out a step-by-step computation we write Eq. (7) in a different form by using the relation $V\Delta t = \Delta s$, thus,

$$-\frac{\Delta \zeta}{\Delta t} = \frac{\Delta f}{\Delta t} + fD + \zeta D + k\zeta$$

The increment of Coriolis parameter

$$\Delta f = \beta \Delta y = \beta V \sin \alpha \, \Delta t \tag{8}$$

is then put into this equation to obtain,

$$\frac{\Delta \zeta}{\Delta t} = -(\beta V \sin \alpha + fD + \zeta D + k\zeta) \quad , \tag{9}$$

where β denotes Rossby parameter, V, the air speed, and α, the direction of the flow measured counterclockwise from local east. It will be feasible to compute the rate of change in the relative vorticity from this equation after making a few further assumptions.

Although Eq. (9) gives the impression that vorticity and divergence can be independent of each other, their relationship presented in a scatter diagram (see Fig. 7) does imply that divergence decreases with increasing vorticity, thus

$$D = -0.48\,\zeta \qquad (10)$$

This coefficient, -0.48, applies for the equatorial Pacific between 5N and 25N where statistics were made. In the southern hemisphere the sign of the coefficient should be reversed because negative vorticity is associated with a convergence. A generalized but simplified relationship between ζ and D may be written as

$$D = -cf\zeta \qquad (11)$$

where f is Coriolis parameter and c, a constant. The latter may be affected by β, V, α, and k in Eq. (9), but we will be keeping this a constant in this paper in order to avoid further complications. From Eq. (10) and the mean value of f at 15N, we have

$$c = \frac{0.48}{f \text{ at } 15N} = \frac{0.48}{3.78 \times 10^{-5}} = 0.13 \times 10^{5} \text{ sec} . \qquad (12)$$

Although the divergence-vorticity relationship expressed by Eq. (11) needs further modification, it would be considerably better than simply assuming either non-divergence or specific divergence values in the low-level atmosphere. By putting Eq. (11) into Eq. (9) we eliminate divergence, thus

$$\frac{\Delta\zeta}{\Delta t} = cf\zeta^{2} + (cf^{2}-k)\zeta - \beta V \sin\alpha . \qquad (13)$$

This equation will permit us to compute the rate of change in relative vorticity if initial

conditions of flow are given.

Since our primary interest is to compute cross-equatorial trajectory, we form rectangular coordinates with the origin at the equator-crossing point, x axis pointing east, and y pointing north. Each trajectory then starts from $x_o = 0$ and $y_o = 0$.

The initial vorticity at the equator may be chosen as a function of the equator-crossing angle α_0 measured from x axis to the velocity vector. A simplified equation can be written as

$$\zeta_0 = -b_0 V_0 \sin \alpha_0 \quad , \tag{14}$$

because a southerly flow tends to be characterized by a negative absolute vorticity advected from the Southern Hemisphere while a northerly flow will have a positive absolute vorticity. Eq. (14) indicates that the initial vorticity is proportional to the north-south component of cross-equatorial wind velocity. From the empirical relationship that $\zeta_0 = -1.0 \times 10^{-5} \sec^{-1}$ when $V_o = 10 \text{ m sec}^{-1}$ and $\alpha_0 = 135^{\circ}$, we estimate b_0 being

$$b_0 = \frac{-\zeta_0}{V_0 \sin \alpha_0} = \frac{1.0 \times 10^{-5} \sec^{-1}}{10 \sin 135^{\circ} \text{m sec}^{-1}} \cong 0.14 \times 10^{-5} \text{m}^{-1} \tag{15}$$

Complete solutions of Eq. (13) require further assumptions of the wind speed and its lateral gradient. Using Riehl's (1954) justification we made the following two assumptions:

$$V = \text{constant} = V_0$$

$$\text{and} \quad \frac{\partial V}{\partial n} = 0 \quad , \tag{16}$$

so as to express relative vorticity

$$\zeta = \frac{V}{r} - \frac{\partial V}{\partial n} \cong \frac{V_0}{r} \tag{17}$$

where r denotes the radius of curvature of the flow.

Through standard procedure we compute both Δx and Δy from

$$x_{n+1} - x_n = \Delta x_n = V_0 \Delta t \cos \alpha_n$$

(18)

$$y_{n+1} - y_n = \Delta y_n = V_0 \Delta t \sin \alpha_n$$

where the suffix n is changed 0, 1, 2, 3 ... to j for each time-interval Δt . The increment of α is expressed by

$$\alpha_{n+1} - \alpha_n = \Delta \alpha_n = \frac{V_0 \Delta t}{r_n} = \zeta_n \Delta t$$

(19)

A number of trajectories of cross-equatorial air under the influence of various parameters were computed in order to determine the air motion after crossing the equator. Presented in Fig. 11 are these trajectories with the cross-equatorial speed of 20 kt which was kept constant as expressed in Eq. (16). The equator crossing angle α was varied as 10°, 50°, 90°, 130°, 150°, and 170°. It should be noted, however, that the trajectories for $\alpha = 0^\circ$ and 180° follow the equator eastward and westward, respectively.

The coefficient k was selected as 2×10^{-5} $\sec^{-1}$ in obtaining the upper figure in which trajectories extend up to about 20N before returning gradually toward the equator in an oscillatory fashion while travelling eastward. It is of interest to find that the maximum northward penetration of the Southern Hemisphere air occurs when the equator-crossing angle is 170°. If it increases by 10° to 180° the air will travel along the equator without deviating either north or south. When α decreases to less than 90° trajectories reach only up to about 8°.

By decreasing the coefficient k to zero, trajectories show dramatic changes resulting in the formation of loops when α exceeds about 150° and also in the returning of the air to the Southern Hemisphere where it started from. A group of such trajectories with varying α is presented in the lower diagram of Fig. 11.

In view of significant changes in the shapes of trajectories when k was changed from zero to 2×10^{-5} $\sec^{-1}$, we may postulate that the equatorial anticyclone presented

earlier will form only if the value of k is approximately equal to 1×10^{-5} sec^{-1} which is very small compared with other estimated values. It is likely that a suppressed low-level overturning over the South Equatorial cold current results in such a small value of k. Over the equatorial regions with warm ocean-surface temperature, the large value of k would not permit a cross-equatorial trajectory to recurve for the formation of an equatorial anticyclone.

In order to evaluate the influence of the cross-equatorial velocity, V_0 upon the shape and the maximum northward penetration of trajectories, Fig. 12 was produced by changing V_o into 10, 20, and 30 kt. It is of extreme interest to find that the size of the anticyclonic loop appearing when k = 0 increases significantly with V_0, while three trajectories with three different velocities remain almost identical when k exceeds $2 \times 10^{-5} sec^{-1}$. That is to say, the cross-equatorial air will follow a trajectory determined mainly by k and not by V when k is larger than $2 \times 10^{-5} sec^{-1}$.

The northward penetration increases significantly with increasing k. This would be a partial reason why Southern Hemisphere air in northern summer penetrates far into northern latitudes over the warm western Pacific and western Atlantic especially when the equator crossing angle is close to 170°. However, the mean crossing angle over the region of the anticyclone formation is about 135°.

Although the results of these numerical computations of trajectory are rather preliminary, they will have a potential value in studying cross-equatorial cloud motions which can now be determined from a series of ATS pictures.

7. A Model of Migratory Equatorial Anticyclones

It was revealed in the previous sections that an organized cross-equatorial flow from the Southern Hemisphere in winter gains its relative anticyclonic vorticity. The effect of β or the northward increase in Coriolis parameter f will overcome that of the vorticity dissipating force especially when k is small. Areas of small k would naturally coincide with oceanic regions with cold sea-surface temperatures. The eastern equatorial Pacific is really qualified for one of the most favorable regions of the formation of equatorial anticyclones.

Presented in Fig. 13 is a model of a migratory equatorial anticyclone which was

established after studies of cloud patterns and velocities over the eastern equatorial Pacific.

During the "Pushing Stage", a large scale flow from the Southern Hemisphere pushes northward, thus producing a convex band of intertropical cloudiness. During this pushing stage the band is pushed as far as 1,000 km to the north. We often observe formation of tropical storms along the zone in which Northern and Southern Hemisphere air begins interacting with large horizontal wind shear and cyclonic relative vorticity.

Within one to three days the flow from the Southern Hemisphere gains sufficient anticyclonic relative vorticity. The flow starts returning southward, thus entering the "recurving stage". The intertropical cloud band shows little change. Tropical depressions formed in the pushing stage tend to move out from the region of the tropical cloud band in this stage.

After a day or so the equatorial anticyclone will be characterized by an enclosed circulation, forming an anticyclone . This stage is called the "Cut-off Stage". During this stage, the anticyclone center is encircled entirely by the air from the Southern Hemisphere.

As soon as a break in the intertropical cloud band takes place, the Northern Hemisphere trade starts flowing to the south of the anticyclonic flow. Then the Northern trade and the flow from the Southern Hemisphere start mixing around the anticyclone center. This stage is called the "Mixing Stage."

After a day or so a significant amount of the northern trade is transported through the southern sectors of the equatorial anticyclone migrating toward the west-northwest. Meanwhile the flow from the Southern Hemisphere keeps pushing the cloud band along the leading edge of the anticyclone. Such a joint push by both northern trade and the flow from the Southern Hemisphere often results in a very intense zone of convergence with cyclonic vorticity. An intense band of intertropical cloudiness located in this zone may be called the "burst band". This proposed term is related to the northwesterly expansion of an intertropical cloud band. In order to emphasize this phenomenon we call this stage the "Burst Stage". This stage lasts only one or two days and then the burst band disintegrates quickly into small fragments or isolated cloud clusters.

After the disintegration of the burst band there still remains a rather intense flow to the south of the equatorial anticyclone center moving in a north to northwesterly direction. This anticyclonic flow is still strong enough to prevent the southeasterly movement of a middle-latitude cold front in the summer hemisphere. A wave on the cold front is observed in this "Interacting Stage." The interaction takes place between a cold front and an equatorial anticyclone which has advected into middle latitudes.

The entire life cycle of an equatorial anticyclone requires about a two-week period. Depending upon the frequency of the anticyclone formation, we often see two anticyclones in different stages of development at the same time over the equatorial northern Pacific, especially in August or September.

8. Structure of a Burst Band

Because the equatorial anticyclones under discussion form over the equatorial eastern Pacific where no upper-air observations are available, it would be very difficult to establish their three-dimensional models. When a burst stage is reached, however, a burst band is located over the equatorial central Pacific where several upper-air stations are in existence.

We shall examine the passage of a strong burst band over Johnston Island located at 16.7N and 169.5W. Shown in Fig. 14 is a time section of various meteorological parameters recorded at the surface. A burst band moved over the station on September 24, 1967 local time. Heavy rain occurred in five separate periods identified in the figure as R1 through R5. The heaviest hourly rain occurring between 6 and 7 local time was 0.75" followed by 0.65" during the following hour. The wind direction shifted to southerlies at the onset of the first rain R1, thus placing most of the burst band inside the southeasterly flow just behind the leading edge of the band. This position of the band coincides with that of the intertropical cloud band in Fig. 2 already discussed. In both cases, therefore, it is the southeasterly flow which converges into cloud bands while the easterly ahead of the line is acting more or less as a barrier to initiate both convergence and cyclonic vorticity.

Surface pressures are not affected by the passage of the burst band. They could be a few tenths of a millibar higher than the average semi-diurnal variation. Surface

temperatures are affected considerably especially during the rain periods. During the five rain periods, the temperature dropped by 3C to 5C. As explained by Riehl (1954) these drops are due to cooling by rain. The fact that the pressure variation is insignificant strongly suggests that it is the shallow layer above the ground which is chilled by rain.

The vertical cross section of winds aloft from Johnston Island for about a 10-day period in September 1967 is shown in Fig. 15. Two burst bands, a weak one on September 17 and the other strong one on September 24-25 Greenwich days, passed over the station as indicated in the figure. It is important to find that each band moving westward was followed by an anticyclonic circulation at about the 10,000-ft level. The anticyclone center at the sea level passed to the northeast of the station. Rather intense outflows associated with these burst bands are seen between 25,000 and 50,000 ft. They are identified as outflow 1 and outflow 2. The latter is combined with another outflow 3 from a large cloud cluster located near the equator at the southwest end of the strong burst band. It is of interest to see that burst band 2 was accompanied by a significant anticyclonic center at about 30,000 ft identified in the figure as H2.

The 300-mb chart in Fig. 16 was completed by plotting rawin winds with black station circles, aircraft winds with square boxes, and high-cloud velocities in arrows with open circles. Large areas of convective clouds are stippled. Groups of streamlines drawn in the chart reveal five centers of outflows, H_2, H_3, H_4, H_5, and H_6. Both H_5 and H_6 are the highs associated with long-wave patterns, however, H_2, H_3, and H_4 are closely related to the accumulative outflow from groups of convective clouds or cloud clusters inside the boundary of each outflow system. Outflows 2 and 3 are more or less inseparable because intense convective activities near the southwest and the northwest ends of the burst band are contributing to the maintenance and intensification of these combined outflow systems. It would be highly desirable to compare the relative position of H_2 and H_3 in both Figs. 15 and 16 for better understanding of four-dimensional characteristics of these outflow systems which need to be expressed in x, y, z, and t coordinates.

Returning to Fig. 15 we must recognize that the vertical transport of low-level momentum takes place only inside convective systems in which moist-adiabatic ascent takes place. A dry-adiabatic process does not permit low-level air to transport its horizontal momentum upward against the more or less moist adiabatic stratification of tropical atmosphere. Strong southerly winds in burst band 2 were measured probably

when balloons were under the influence of such convective clouds.

It should be emphasized that the time variation of winds aloft at a single station is related to : 1) the synoptic flow patterns of wind systems, 2) their development and decay, and 3) their migratory velocities.

9. An Example of Equatorial Anticyclones Over the Tropical Pacific

To varify the proposed model of equatorial anticyclones efforts are being made to complete analyses of surface and 300-mb charts over the equatorial Pacific for the entire month of September 1967.

Tracks of two major equatorial anticyclones, A_1 and A_2 appear in Fig. 17. Note that each anticyclone lived over 10 days while travelling with the westward velocity component. The travelling speed varied between about 5 to 10 degrees per day, which is comparable to that of hurricanes and easterly waves.

A question might arise as to why the eastern tropical Pacific is favorable for such anticyclone formation. One reason being the cold ocean-surface temperature as studied extensively by Bjerknes (1966) who pointed out the importance of the South Equatorial cold current extending from off the Pacific coast of South America to the equator. To confirm the existence of the cold current during the period of our analysis all ship reports during a three-day period, September 17-19, were plotted on a composite chart of Fig. 18. It will be seen that a tongue of cold surface water was dominating the equatorial region.

Such a cold ocean-surface temperature would suppress vertical mixing of the air inside the friction layer. That is to say, the value of k in Fig. 10 and Eq. (4) is expected to be very small over the region of this cold current. This means that the cross-equatorial flow will quickly gain anticyclonic relative vorticity as it travels with a northerly component, thus decreasing ζ with time. Over the area of high ocean-surface temperature, however, the resulting convection and vertical mass exchange inside the friction layer tend to dissipate the relative vorticity so that an anticyclone development will be suppressed.

We shall now examine surface analyses corresponding to the six stages of an anticyclone development. Figure 19, including six surface charts covering longitudes

150E through 90W, was drawn by plotting all land-station reports for 00Z and ship reports for 18Z, 00Z, and 06Z. Areas of large nephsystems were copied from ESSA's mosaic pictures reduced to the map scale. Surface streamlines were then drawn taking surface winds and cloud velocities from ATS-I picture analyses into consideration. No cloud velocities were plotted in the figure because they were computed tentatively without correcting the mis-synchronization of ATS scan lines which occurred shortly before the spring and autumnal equinoxes of 1967. We have succeeded, however, in correcting the mis-synch for the September 18 case which was used extensively in this report.

The top chart for September 12 includes anticyclone A_1 in its cut-off stage and A_2 in the pushing stage. Two tropical storms N (Nanette) and M (Monica) are forming simultaneously inside an intertropical cloud band along the leading edge of the southwesterly flow from the Southern Hemisphere. Near the eastern end of the intertropic cloud band associated with anticyclone A_1, we find a very weak vortex identified as P. In case of these examples of vortex formations a large number of vortices were found to form in the cloud band accompanied by an anticyclone in its pushing stage. This mode of vortex formation will correspond to Fett's (1968) second category and also to Erickson and Fritz's (1965) type of formations. A well-developed storm S, hurricane Sarah, near Johnston Island, originated from a weak easterly-wave disturbance and is now travelling westward. Sarah's formation would be in Fett's second category studied intensively by Yanai (1961 and 1968).

The second chart for 00Z, September 16, shows anticyclone A_1, already in the burst stage, and A_2 in the recurving stage. It should be pointed out that both storms N and M are moving away from their nesting band of intertropical cloudiness. Due to their locations over warm equatorial counter current they are maintaining their features of tropical storms. Seen to the southwest of anticyclone A_1 is a weak burst band along which is observed moderate cyclonic curvature in streamlines. Hurricane Sarah is moving toward the western edge of the chart.

On the third chart for 00Z, September 20, Sarah is seen in the northwest corner of the chart and anticyclone A_1 is interacting with a cold front in the middle latitudes. A weak vortex P is still visible near Hawaii. Of interest is an evidence of complete

separation of tropical storms N and M from the intertropical cloud band north of A_2, which has been reestablished into a thin band. Anticyclone A_1 in its cut-off stage is moving westward steadily.

The fourth chart for 00Z, September 24, indicates that anticyclone A_2 has entered its mixing stage characterized by an injection of northern trade into the anticyclone circulation. Two tropical storms N and M are weakening rapidly, while an intertropical cloud band to their south becomes wider, extending toward the south quadrant of hurricane Beulah over Mexico.

The dramatic burst stage of anticyclone A_2 is seen in the fifth chart for 00Z, September 25. A burst band which has passed Johnston Island has already been discussed in the previous section. Seen behind the burst band is a well-defined anticyclonic circulation which might have been analyzed not as an anticyclone but as a noise if there were no satellite data and no circulation model. Over the eastern half of the chart, tropical storm N is weakening further. Meanwhile, the distance from her sister storm M increased considerably.

The last chart for 00Z, September 26, shows anticyclone A_2 in its interacting stage. Note that the southward movement of a cold front has been slowed down in the region of interaction. Both Beulah and Monica merged to form a large, but weak tropical vortex centered on the Pacific coast of Mexico. A dissipating tropical storm Nanette is still seen near the center of the chart.

10. Conclusions

Detailed analyses of data-scarce regions of the eastern tropical Pacific revealed that satellite data can be effectively used in determining the scales and the modes of the tropical circulation. Particularly, the use of ATS pictures in determining fields of cloud velocities resulted definitely in a breakthrough in understanding dynamical aspects of tropical circulations.

As a result of this study, it is concluded that the tropical nephsystems larger than a cloud cluster are accompanied by definite flow fields. These fields are mostly cyclonic and convergent, giving an impression that the frictional convergence is one of the most important driving mechanisms for the formation and the maintenance of cloud clusters

and intertropical cloud bands.

It should be emphasized also that the cloud velocities determined from ATS pictures can be used in evaluating various dynamical parameters such as advection, frictional coupling, etc.

In the light of these results, it would be proper to recommend an organized effort of tropical analyses by collecting all existing synoptic, land and ship data in addition to satellite pictures. These efforts might or are likely to develop into a second look at "tropical synoptic meteorology" as well as "tropical mesometeorology".

REFERENCES

Bjerknes, J., 1966: A possible response of the atmospheric Hadley circulation to equatorial anomalies of ocean temperature. Tellus, 18, 820-829.

Cressman, G. C., 1948: Studies of upper-air conditions in low latitudes. Dept. Meteor., Univ. Chicago, Misc. Rep. 24, Part II, 68-103.

Erickson, C.O., and S. Fritz, 1965: Early history of tropical storm Katherine, 1963. Mo. Wea. Rev., 93, 145-153.

Fett, R. W., 1968: Typhoon formation within the zone of the intertropical convergence. Mo. Wea. Rev., 94, 9-18.

Fujita, T. and D. Bradbury, 1968: Computation of height and velocity of clouds from dual, whole-sky, time-lapse picture sequences. SMRP Research Paper No. 70, 17 pp. (Copies may be obtained from the Department of Geophysical Sciences, The University of Chicago).

Godshall, F.A., 1968: Intertropical convergence zone and mean cloud amount in the tropical Pacific Ocean. Mo. Wea. Rev., 96, 172-175.

Gordon, A. H. and R. C. Taylor, 1966: Lagrangian dynamics and low latitude weather. Hawaii Institute of Geophysics, Univ. of Hawaii, HIG-66-12. 32 pp. (Copies may be obtained from the University of Hawaii).

Kornfield, J., A. F. Hasler, K. J. Hanson, and V. E. Suomi, 1967: Photographic cloud climatology from ESSA III and V computer produced mosaics, Bull. Amer. Meteor. Soc., 48, 878-883.

Palmer, C. E., 1952: Tropical meteorology. Quart. J. R. Met. Soc., 78, 126-164.

Petterssen, S., 1956: Weather Analysis and Forecasting. Vol. 1. McGraw-Hill Co., New York, 428 pp.

Riehl, H., 1954: Tropical Meteorology. McGraw-Hill Co., New York, 392 pp.

Yanai, M., 1961: A detailed analysis of typhoon formation. J. Meteor. Soc. Japan, 39, 186-214.

_____, 1968: Evolution of a tropical disturbance in the Caribbean Sea region. J. Meteor. Soc. Japan, 46, 86-109.

VELOCITY OF LOW CLOUDS
1948-2152 Z, SEPT 17, 1967

← 10kt   ← 20kt   ← 30kt
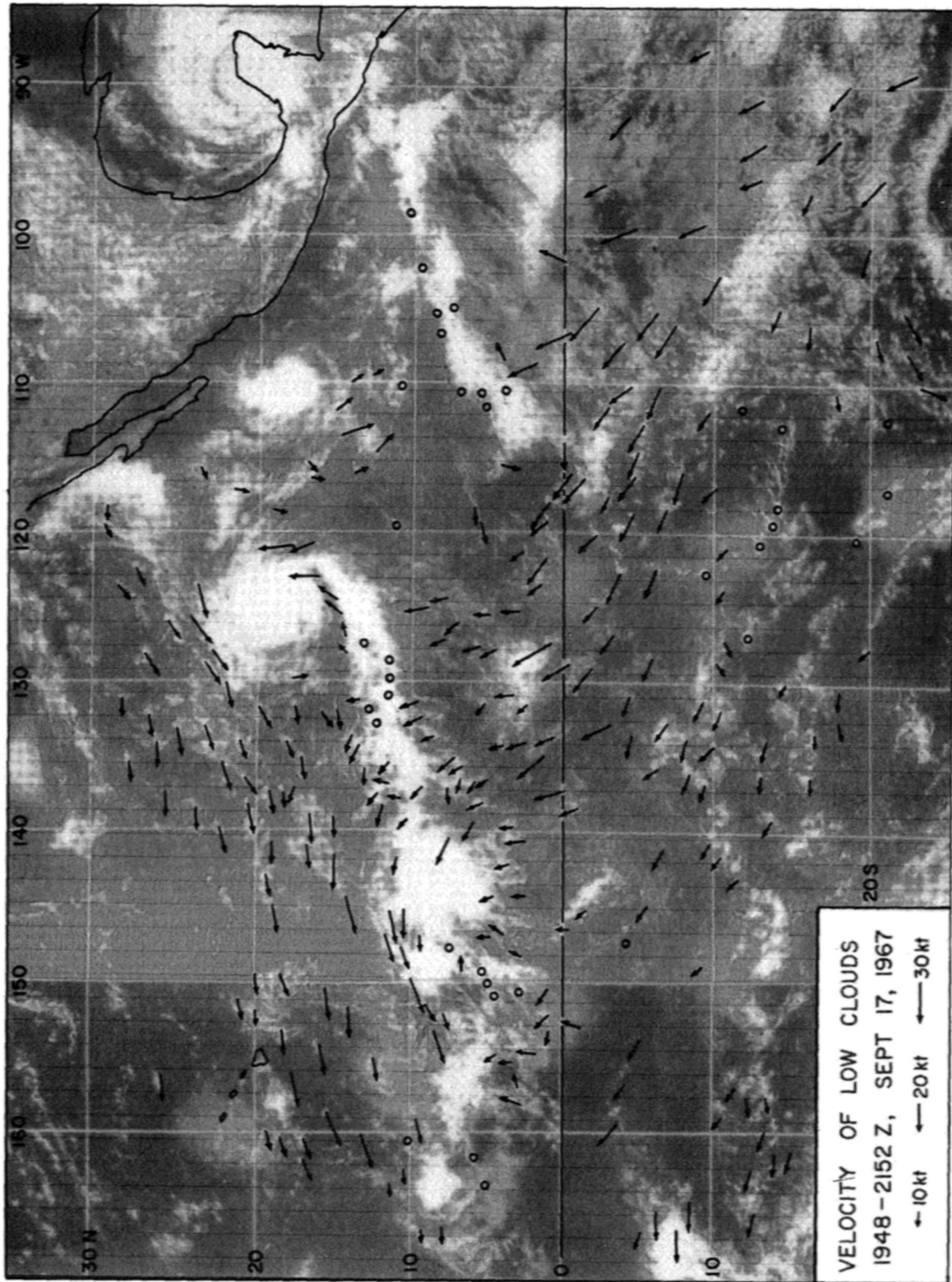
Fig. 1. Velocities of low clouds over the eastern Pacific, plotted on an ESSA digital mosaic on Mercator Projection. Velocities were obtained from six ATS-1 pictures taken at about 25-min intervals.
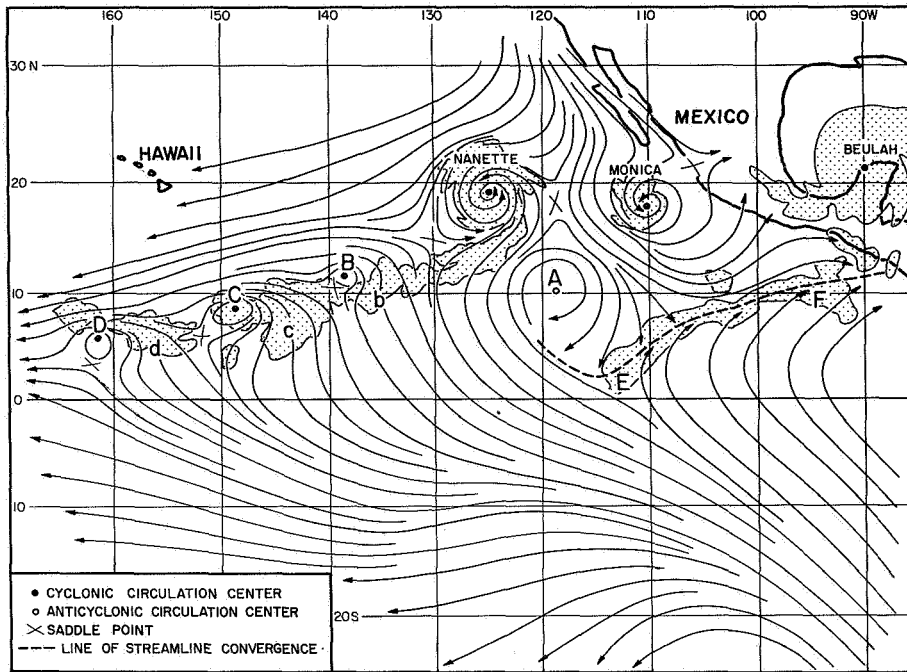
Fig. 2. Streamlines of low-cloud velocities drawn from velocity vectors in Fig. 1.
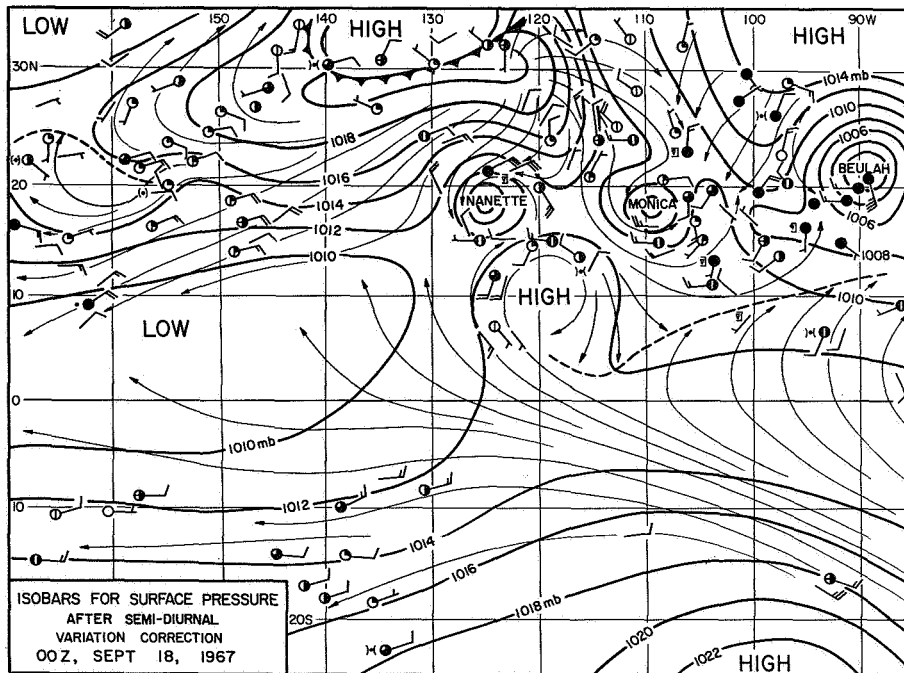
Fig. 3. Surface chart for 00Z, September 1967, about three hours after the time of the velocity computation in Fig. 1. Note that an anticyclone depicted by streamlines in Fig. 2 appears clearly in this surface map. Ship-reported winds at 1800Z on the 17th and 0600Z on the 18th were entered without station circles.
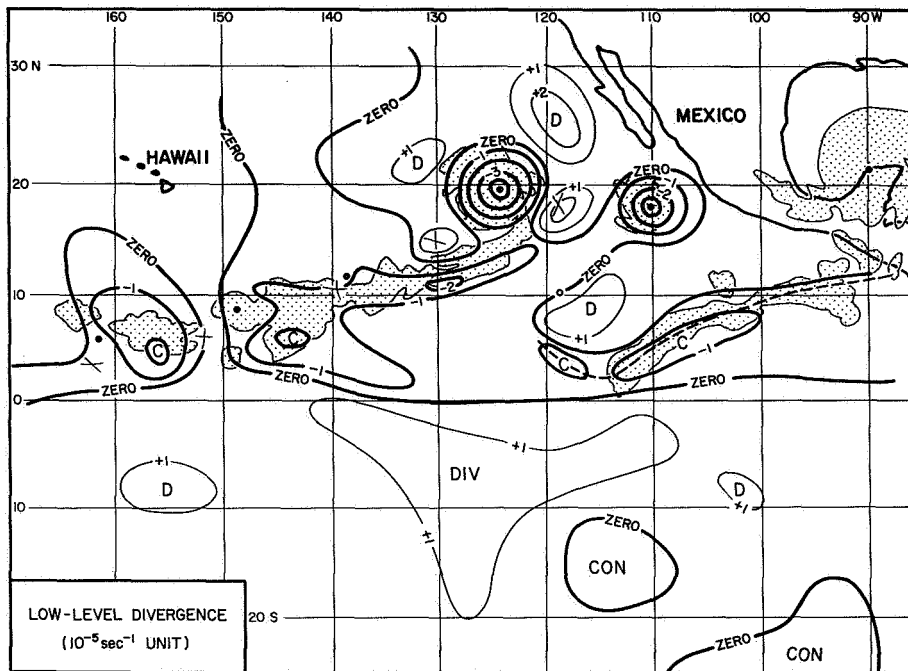
Fig. 4. Divergence of low-cloud velocities in Fig. 1. As expected, the areas of inter-tropical nephsystems are characterized by fields of convergence.
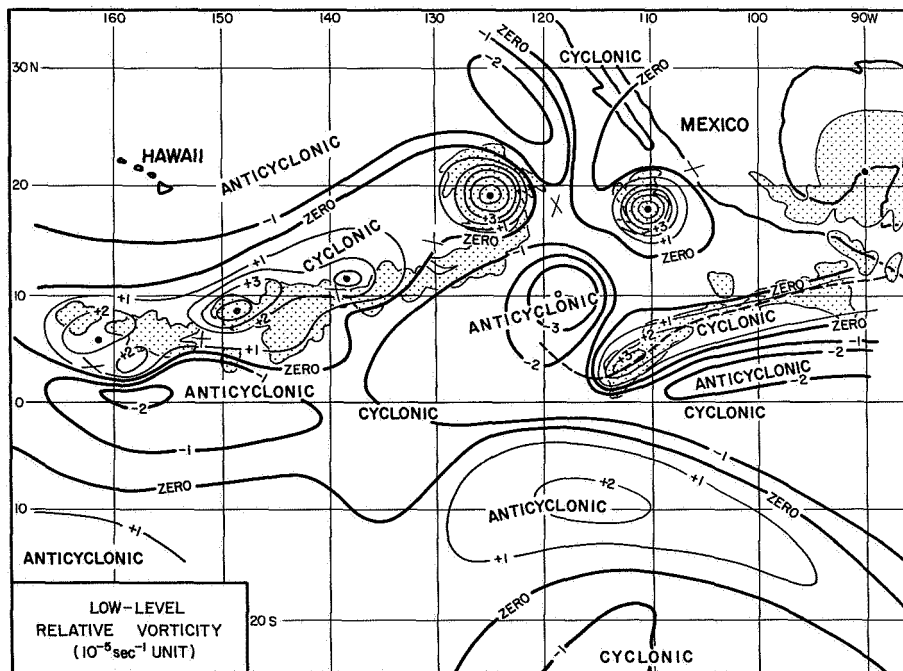
Fig. 5. Relative vorticity of low-cloud velocities in Fig. 1. Note that the areas of nephsystems correspond to those of large relative vorticity.
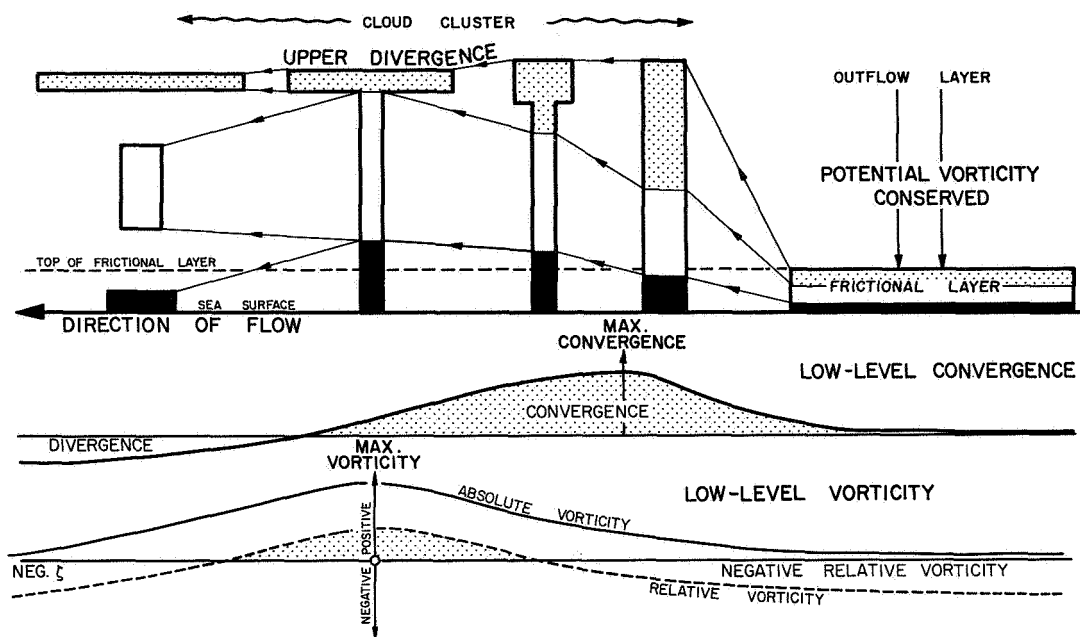
Fig. 6. Mesoscale correspondence between convergence and vorticity advection maxima. Since the frictional layer is mixed, the division of the layer into three sub-layers, top, middle, and bottom, is nearly schematic.
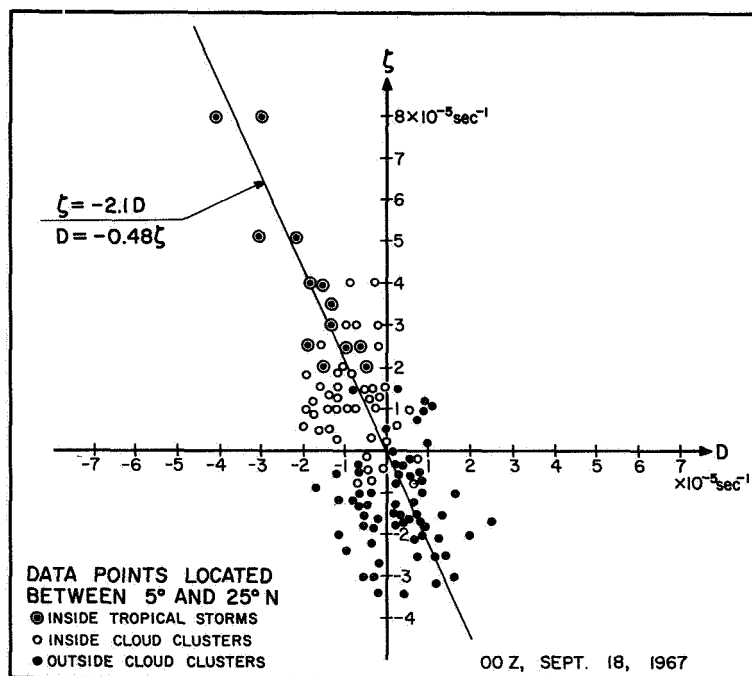
Fig. 7. A scatter diagram showing a linear relationship between divergence and relative vorticity. Data points are located inside a zonal belt between 5N and 25N bounded by 90W and 170W.
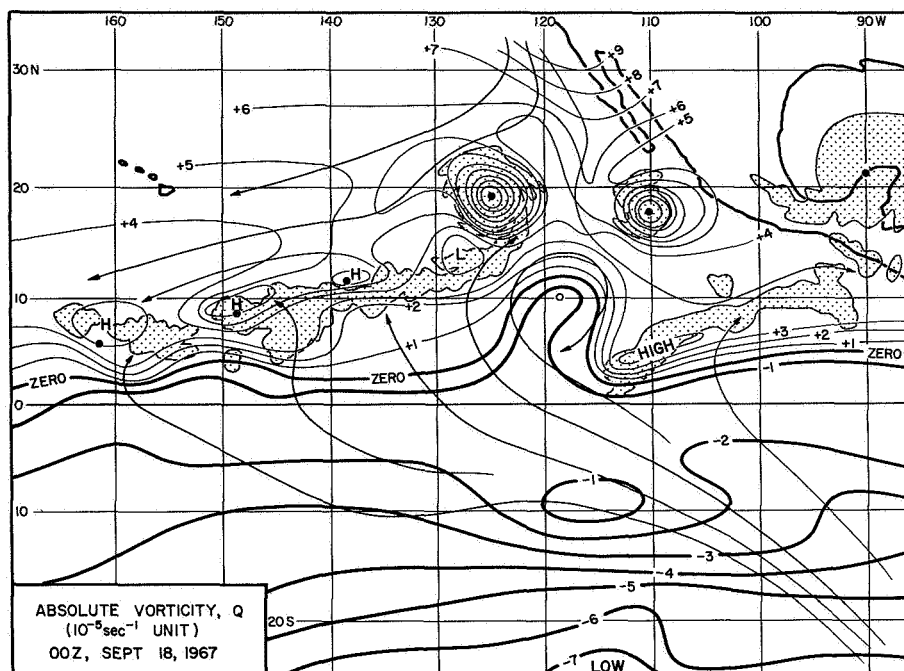
Fig. 8. Absolute vorticity obtained by adding Coriolis parameter to the relative vorticity in Fig. 5.
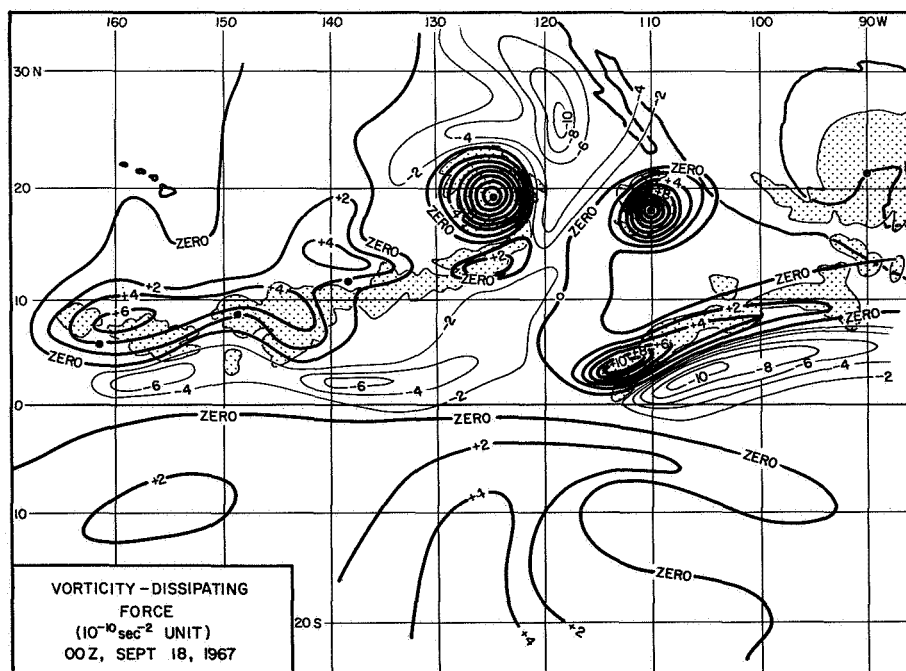
Fig. 9. Vorticity-dissipating force defined by Eq. (3) and computed entirely from ATS cloud pictures. No synoptic data were used in the computation.

Fig. 11. Trajectories of cross-equatorial air computed by changing both the vorticity-dissipating force and the equator crossing angle. Trajectories vary significantly with these input parameters.
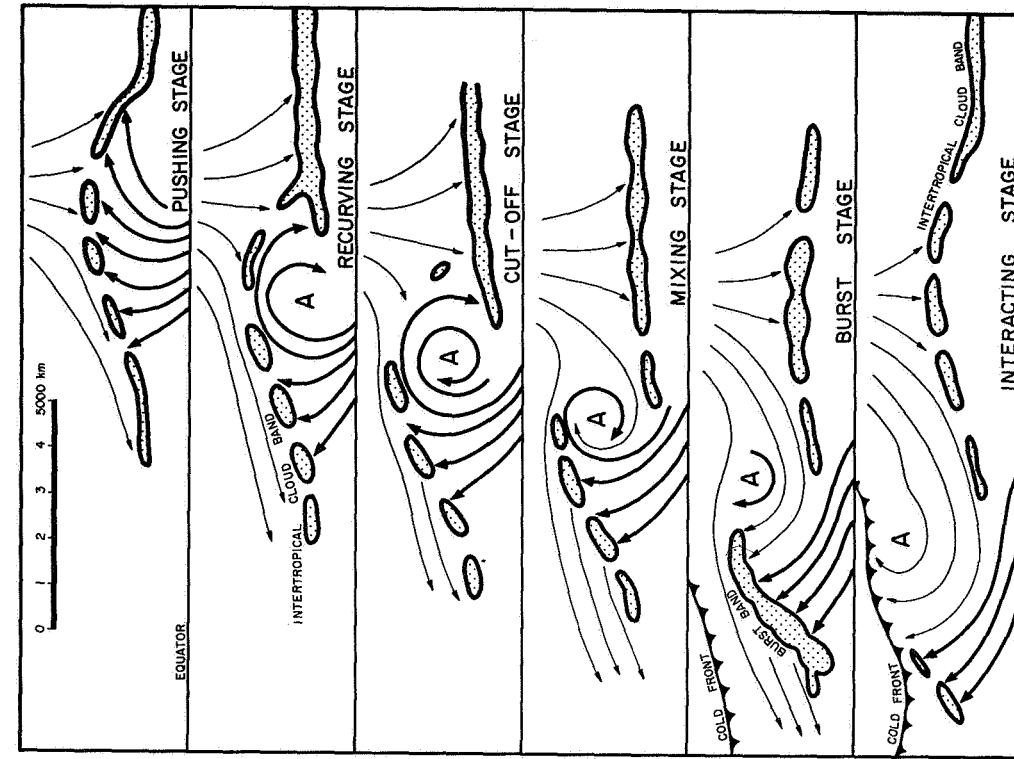

Fig. 10. Scatter diagram relating the vorticity-dissipating force with relative vorticity. The entire area of Fig. 1 was used in determining grid-point data appearing in this diagram. It should be emphasized that this diagram was constructed based on ATS pictures only.

Fig. 13. A proposed model of an equatorial anticyclone in six stages. An example corresponding to each stage is shown in Fig. 19.
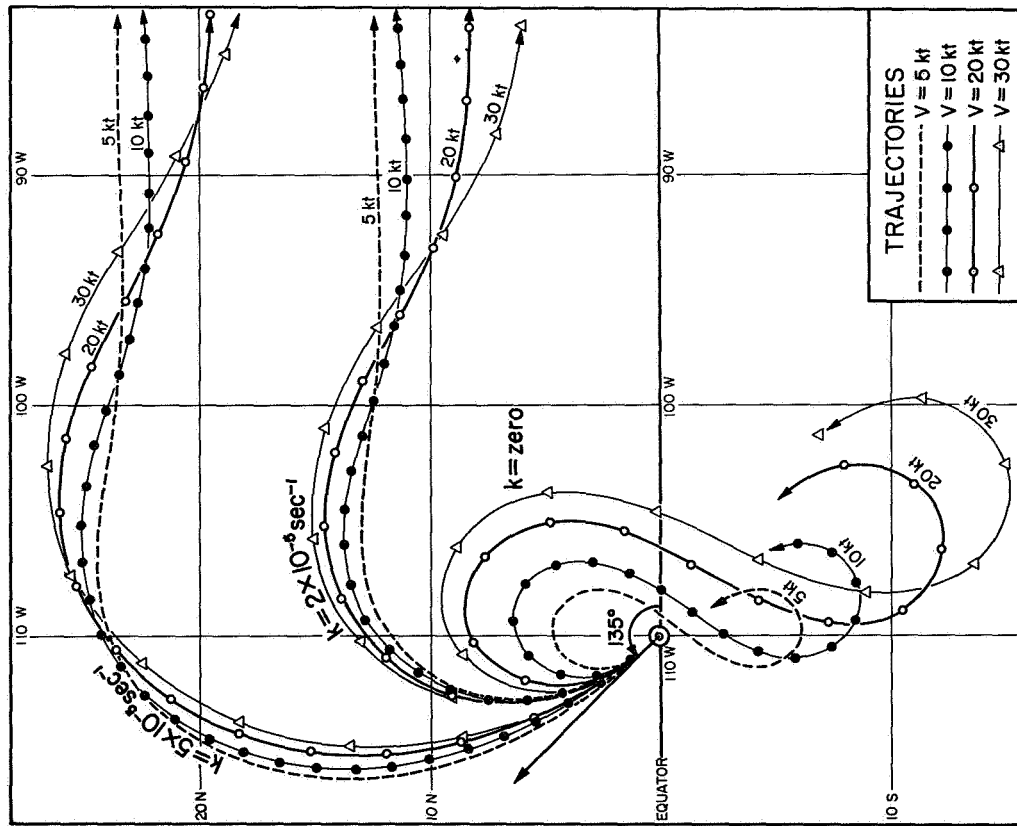
Fig. 12. Influences of the cross-equatorial velocity which was changed from 5 to 30 kt. Unless k is very small, trajectories change very little according to the velocity variation within this range.
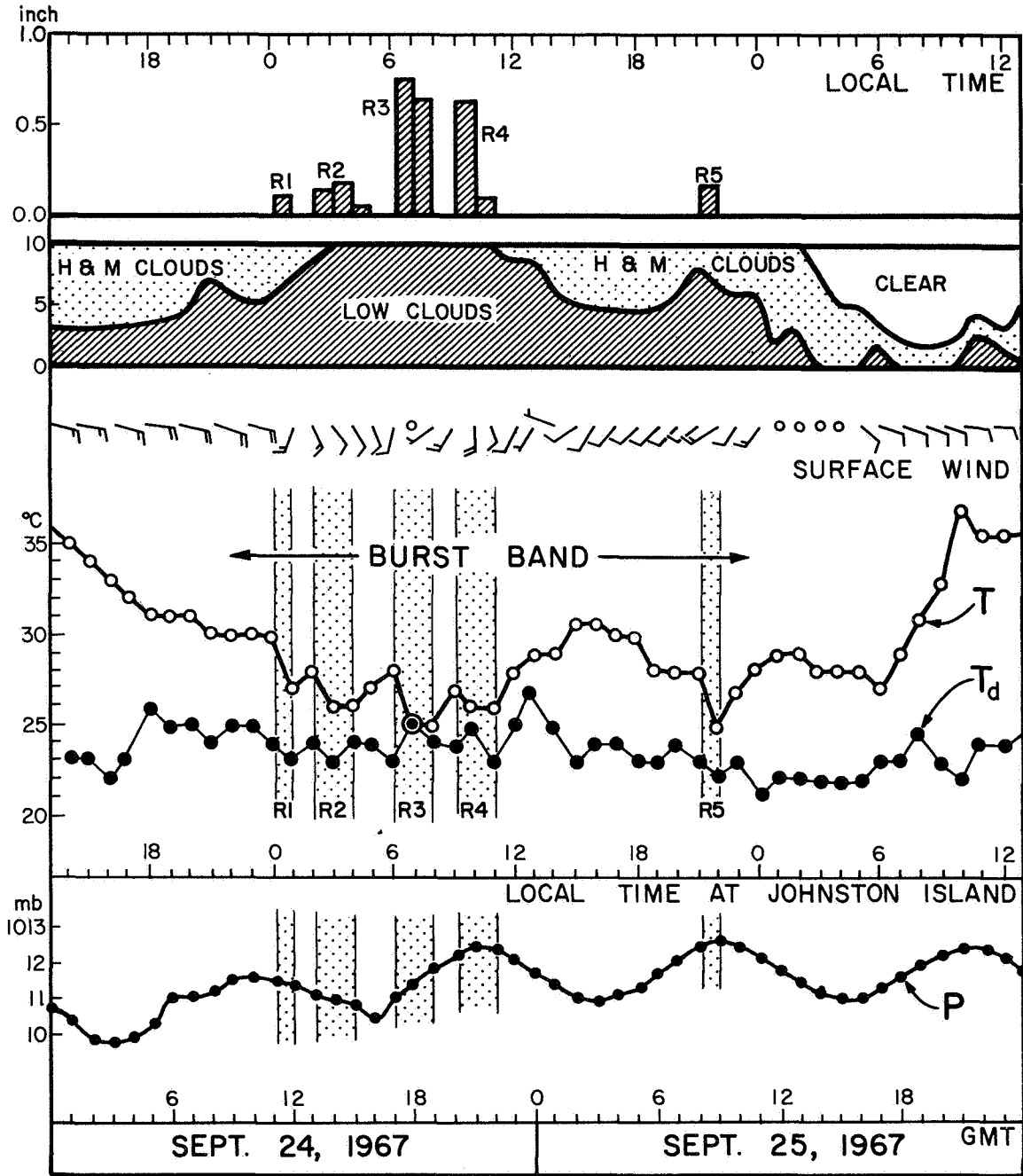
Fig. 14. Passage of a burst band at Johnston Island, 16.7N and 169.5W on September 24-25, 1967. During the passage of the band, rain occurred in five separate periods, producing 0.10, 0.31, 1.40, 0.73, and 0.15 inches, respectively, with a total of 2.69 inches. During each of these rain periods air temperature dropped several degrees.
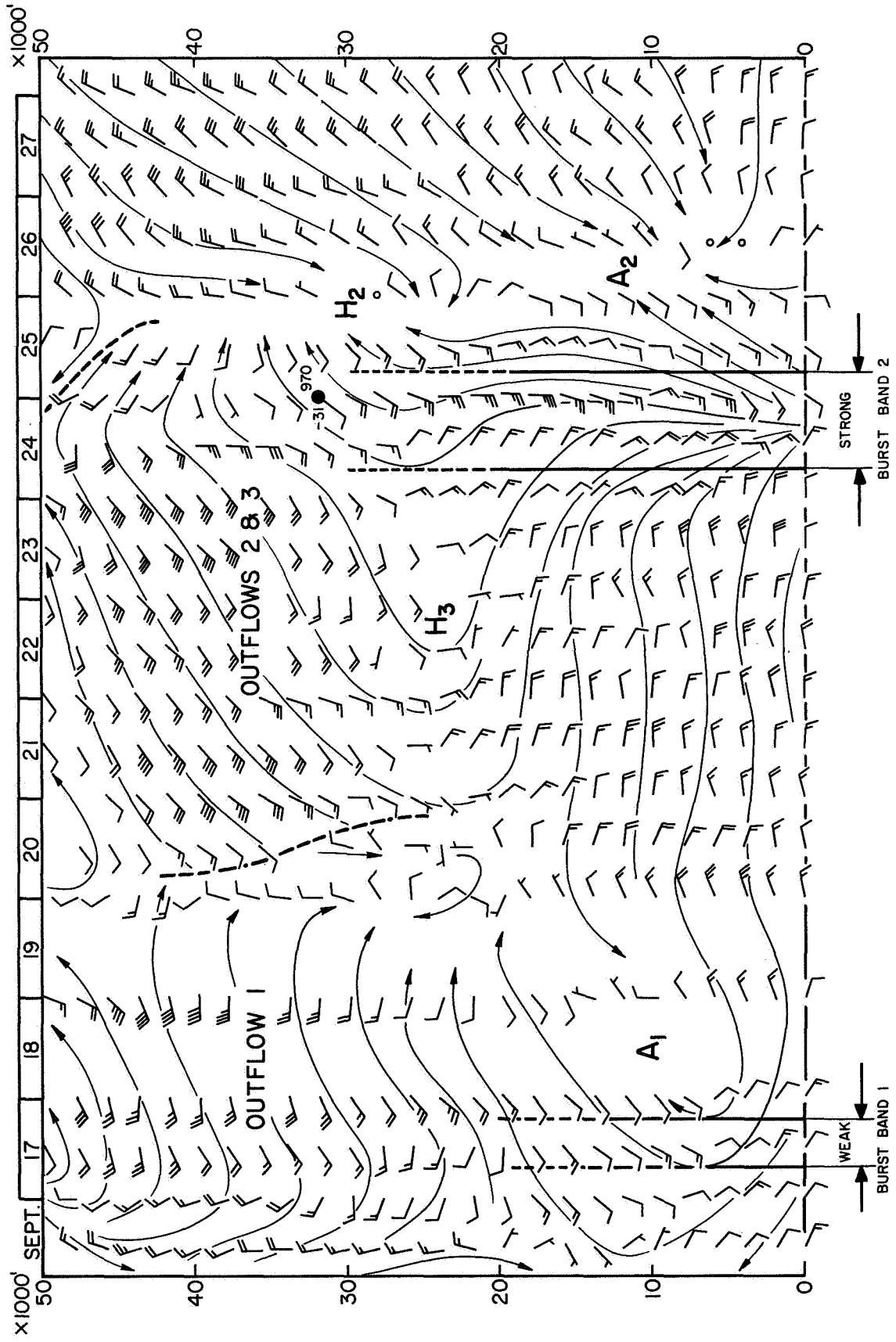
Fig. 15. A vertical time cross section at Johnston Island between September 16 and 28, 1967 when two burst bands passed over the station.
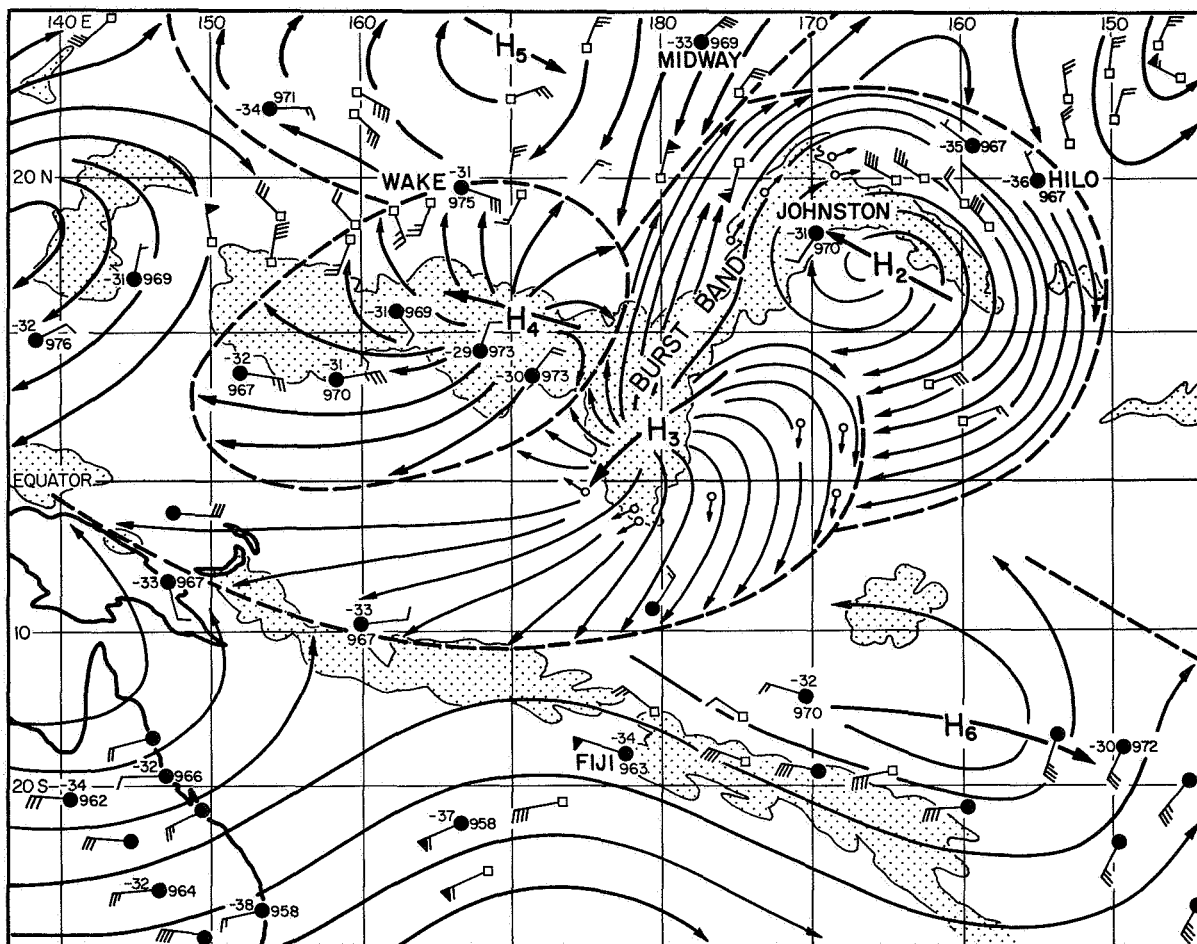
Fig. 16. 300-mb chart for 0000Z, September 25, 1967, when a strong burst band passed over Johnston Island. There were three outflow highs, H_2, H_3, and H_4 which were moving, respectively, from SE, NE, and ESE. Two anticyclone centers, H_5 and H_6 were moving from WNW. Rawin and aircraft data were plotted with regular wind barbs attached to black circles and open squares, respectively. ATS cloud velocities are shown with short arrows. Shown with curved lines with arrow heads are stream lines and the velocities of highs.
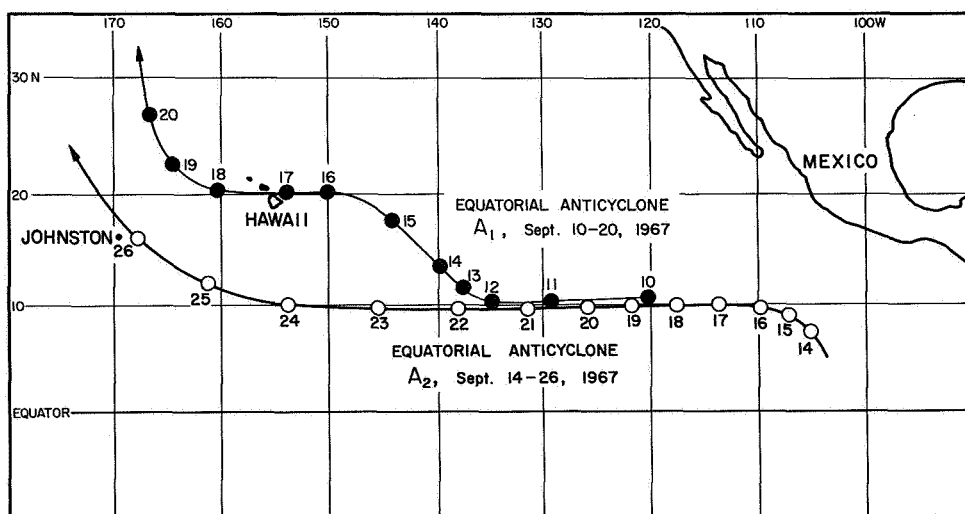

Fig. 17. Tracks of two equatorial anticyclones, A_1 and A_2, which originated to the north of the equator, south of Baja, California. They were tracked for 10 to 14 days until disappearing in the central Pacific.
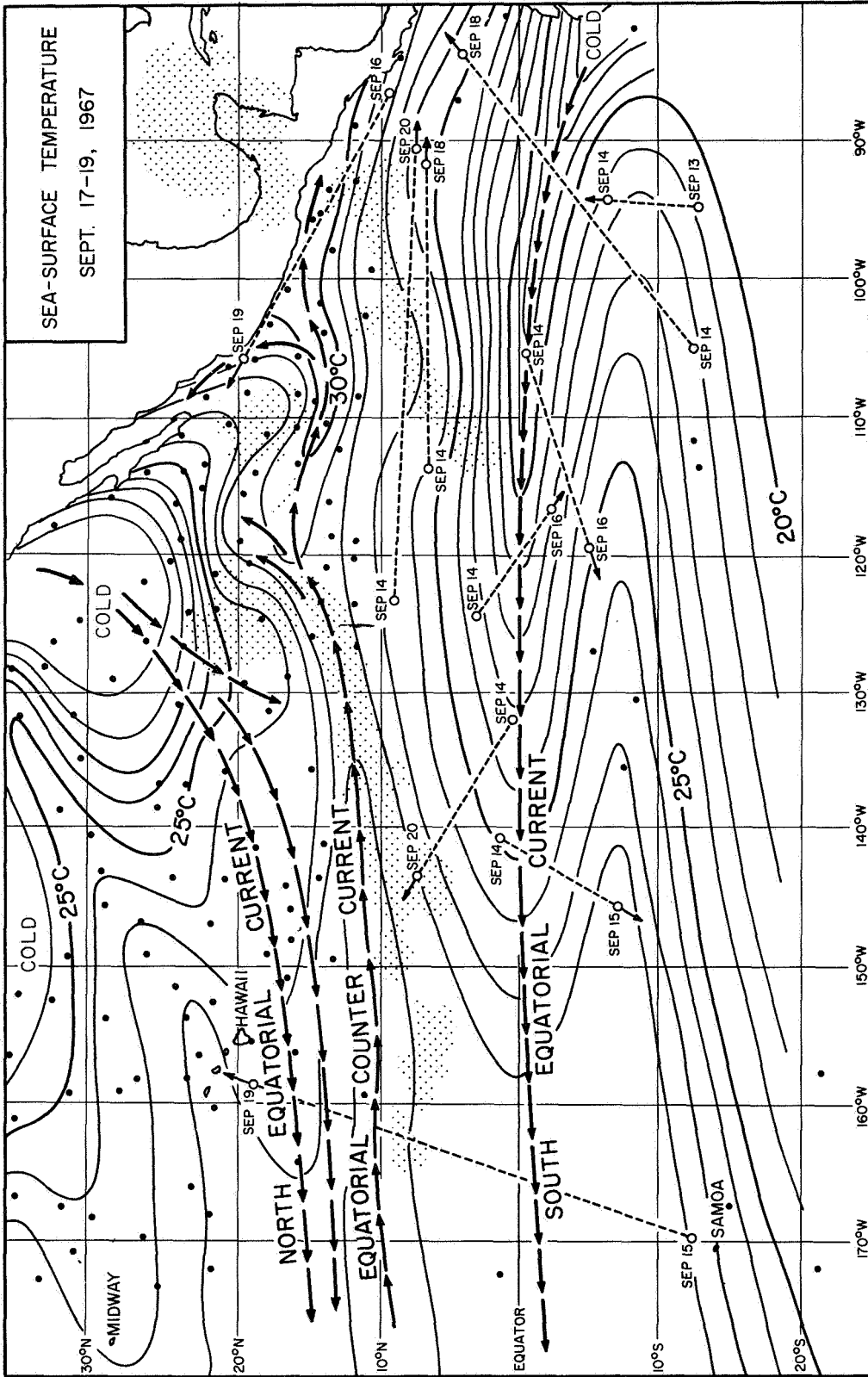
Fig. 18. A composite sea-surface temperature chart for a three-day period, September 17-19, 1967. The temperature contrast between the South Equatorial Current and the Equatorial Counter Current, as large as 12C along 100W, gradually decreases to about 2C to the south of Hawaii.
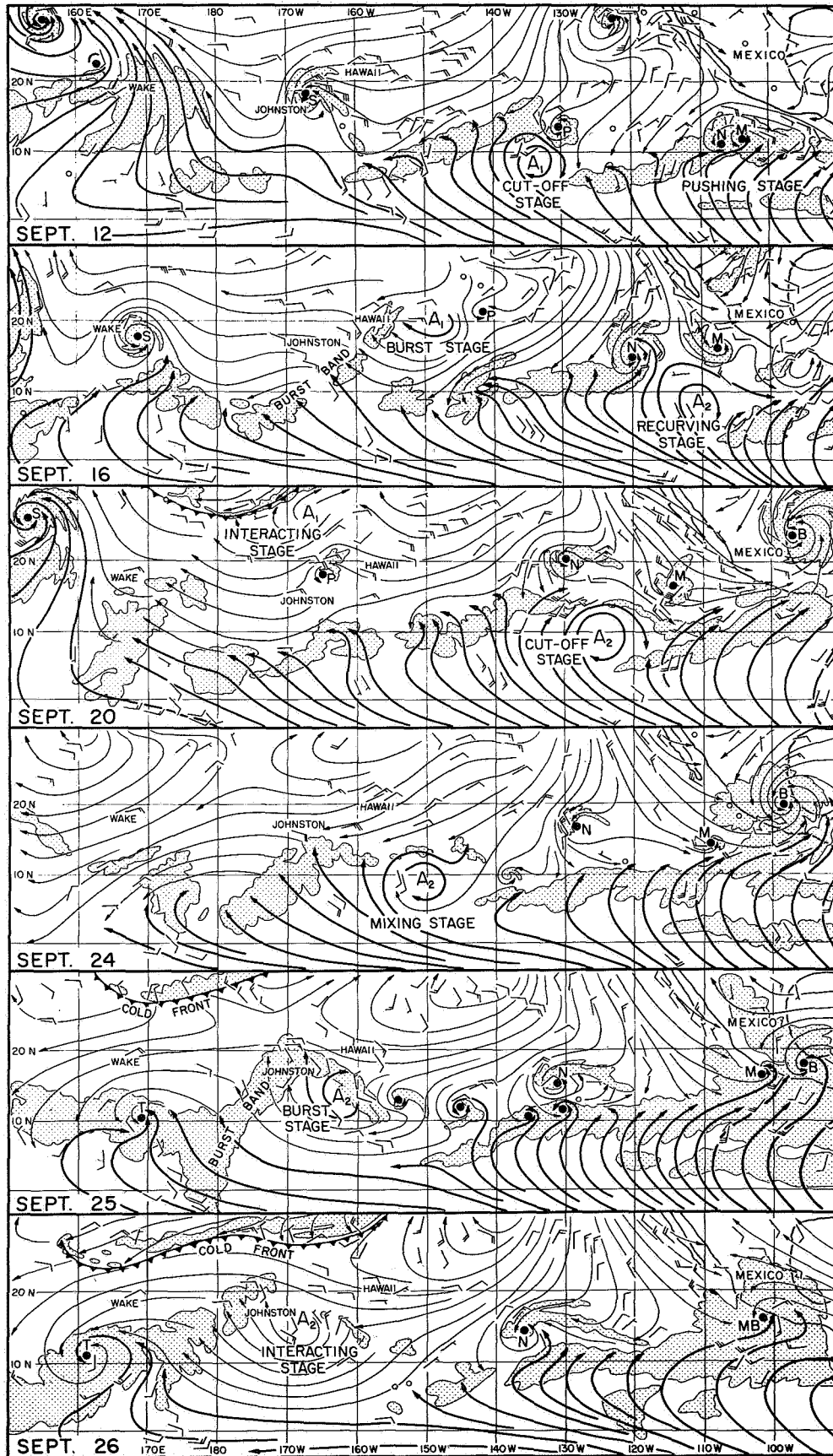
Fig. 19. An example of six stages of an equatorial anticyclone over the north equatorial Pacific. September 12-26, 1967.

MESOMETEOROLOGY PROJECT - - - RESEARCH PAPERS

(Continued from front cover)

42. A Study of Factors Contributing to Dissipation of Energy in a Developing Cumulonimbus - Rodger A. Brown and Tetsuya Fujita

43. A Program for Computer Gridding of Satellite Photographs for Mesoscale Research - William D. Bonner

44. Comparison of Grassland Surface Temperatures Measured by TIROS VII and Airborne Radiometers under Clear Sky and Cirriform Cloud Conditions - Ronald M. Reap

45. Death Valley Temperature Analysis Utilizing Nimbus I Infrared Data and Ground-Based Measurements - Ronald M. Reap and Tetsuya Fujita

46. On the "Thunderstorm-High Controversy" - Rodger A. Brown

47. Application of Precise Fujita Method on Nimbus I Photo Gridding - Lt. Cmd. Ruben Nasta

48. A Proposed Method of Estimating Cloud-top Temperature, Cloud Cover, and Emissivity and Whiteness of Clouds from Short- and Long-wave Radiation Data Obtained by TIROS Scanning Radiometers - T. Fujita and H. Grandoso

49. Aerial Survey of the Palm Sunday Tornadoes of April 11, 1965 - Tetsuya Fujita

50. Early Stage of Tornado Development as Revealed by Satellite Photographs - Tetsuya Fujita

51. Features and Motions of Radar Echoes on Palm Sunday, 1965 - D. L. Bradbury and T. Fujita

52. Stability and Differential Advection Associated with Tornado Development - Tetsuya Fujita and Dorothy L. Bradbury

53. Estimated Wind Speeds of the Palm Sunday Tornadoes - Tetsuya Fujita

54. On the Determination of Exchange Coefficients: Part II - Rotating and Nonrotating Convective Currents - Rodger A. Brown

55. Satellite Meteorological Study of Evaporation and Cloud Formation over the Western Pacific under the Influence of the Winter Monsoon - K. Tsuchiya and T. Fujita

56. A Proposed Mechanism of Snowstorm Mesojet over Japan under the Influence of the Winter Monsoon - T. Fujita and K. Tsuchiya

57. Some Effects of Lake Michigan upon Squall Lines and Summertime Convection - Walter A. Lyons

58. Angular Dependence of Reflection from Stratiform Clouds as Measured by TIROS IV Scanning Radiometers - A. Rabbe

59. Use of Wet-beam Doppler Winds in the Determination of the Vertical Velocity of Raindrops inside Hurricane Rainbands - T. Fujita, P. Black and A. Loesch

60. A Model of Typhoons Accompanied by Inner and Outer Rainbands - Tetsuya Fujita, Tatsuo Izawa., Kazuo Watanabe and Ichiro Imai

61. Three-Dimensional Growth Characteristics of an Orographic Thunderstorm System - Rodger A. Brown

62. Split of a Thunderstorm into Anticyclonic and Cyclonic Storms and their Motion as Determined from Numerical Model Experiments - Tetsuya Fujita and Hector Grandoso

63. Preliminary Investigation of Peripheral Subsidence Associated with Hurricane Outflow - Ronald M. Reap

64. The Time Change of Cloud Features in Hurricane Anna, 1961, from the Easterly Wave Stage to Hurricane Dissipation - James E. Arnold

65. Easterly Wave Activity over Africa and in the Atlantic with a Note on the Intertropical Convergence Zone during Early July 1961 - James E. Arnold

66. Mesoscale Motions in Oceanic Stratus as Revealed by Satellite Data - Walter A. Lyons and Tetsuya Fujita

67. Mesoscale Aspects of Orographic Influences on Flow and Precipitation Patterns - Tetsuya Fujita

68. A Mesometeorological Study of a Subtropical Mesocyclone -Hidetoshi Arakawa, Kazuo Watanabe, Kiyoshi Tsuchiya and Tetsuya Fujita

69. Estimation of Tornado Wind Speed from Characteristic Ground Marks - Tetsuya Fujita, Dorothy L. Bradbury and Peter G. Black

70. Computation of Height and Velocity of Clouds from Dual, Whole-Sky, Time-Lapse Picture Sequences - Dorothy L. Bradbury and Tetsuya Fujita

71. A Study of Mesoscale Cloud Motions Computed from ATS-I and Terrestrial Photographs - Tetsuya Fujita, Dorothy L. Bradbury, Clifford Murino and Louis Hull

72. Aerial Measurement of Radiation Temperatures over Mt. Fuji and Tokyo Areas and Their Application to the Determination of Ground- and Water-Surface Temperatures - Tetsuya Fujita, Gisela Baralt and Kiyoshi Tsuchiya

73. Angular Dependence of Reflected Solar Radiation from Sahara Measured by TIROS VII in a Torquing Maneuver - Rene Mendez.

74. The Control of Summertime Cumuli and Thunderstorms by Lake Michigan During Non-Lake Breeze Conditions - Walter A. Lyons and John W. Wilson

75. Heavy Snow in the Chicago Area as Revealed by Satellite Pictures - James Bunting and Donna Lamb

76. A Model of Typhoons with Outflow and Subsidence Layers - Tatsuo Izawa

* out of print